Earth Radiation Budget and Cloudiness Simulations with a General Circulation Model

HARSHVARDHAN,*,+,** DAVID A. RANDALL,@ THOMAS G. CORSETTI+,* AND DONALD A. DAZLICH||,@

*Goddard Laboratory for Atmospheres, NASA/GSFC, Greenbelt, Maryland
+Dept. of Meteorology, University of Maryland, College Park, Maryland
||Centel Federal Services Corp., NASA/GSFC, Greenbelt, Maryland

(Manuscript received 11 August 1988, in final form 4 January 1989)

ABSTRACT

The UCLA/GLA general circulation model has been endowed with new parameterizations of solar and terrestrial radiation, as well as new parameterized cloud optical properties. A simple representation of the cloud liquid water feedback is included. We have used the model and several observational datasets to analyze the effects of cloudiness on the Earth's radiation budget.

Analysis of January and July results obtained with the full model shows that the simulated Earth radiation budget is in reasonable agreement with Nimbus 7 data. The globally averaged planetary albedo and outgoing longwave radiation are both slightly less than observed. A tropical minimum of the outgoing longwave radiation is simulated, but is weaker than observed. Comparisons of the simulated cloudiness with observations from ISCCP and HIRS2/MSU show that the model overpredicts subtropical and midlatitude cloudiness.

The simulated cloud radiative forcings at the top of the atmosphere, at the Earth's surface, and across the atmosphere are discussed, and comparisons are made with the limited observations available. The simulated atmospheric cloud radiative forcing (ACRF) is comparable in magnitude to the latent heating. We have compared the clear-sky radiation fields obtained using Methods I and II of Cess and Potter; the results show significant differences between the two methods, primarily due to systematic variations of the cloudiness with time of day.

An important feature of the new terrestrial radiation parameterization is its incorporation (for the first time in this GCM) of the effects of the water vapor continuum. To determine the effects of this change on the model results, we performed a numerical experiment in which the effects of the water vapor continuum were neglected. The troposphere warmed dramatically, and shallow convection weakened, and the radiative effects of the clouds were significantly enhanced.

1. Introduction

Since radiation is the only mechanism by which the Earth can gain or lose energy, the climate is determined, in a gross sense, by the radiation balance at the top of the atmosphere. This balance depends on the insolation and the spectrally dependent optical properties of the atmosphere and the Earth's surface. To a remarkable degree, these optical properties are determined by the distribution of water in its various forms. The most optically important of the variable atmospheric gases is water vapor, and the most optically important atmospheric aerosols are clouds of ice and/or liquid water. The optical properties of the Earth's surface are dominated by the oceans, and fluctuate primarily due to changes in the distributions of snow and ice. In these ways, the Earth's climate is strongly influenced by moisture. We cannot understand climate without understanding the hydrologic cycle.

Cloudiness, in particular, greatly complicates the dynamics of climate. The clouds are reflecting blankets; they can cool the Earth by scattering sunlight back to space, or they can warm it by trapping terrestrial radiation. It is not clear a priori whether cooling or warming wins out, or how the cloudiness would change in response to a climate change. Most early general circulation models (GCMs) could not be used to explore these questions, because they included only prescribed zonally uniform clouds. This drastic simplifying assumption was motivated by the mistaken belief that cloud–radiation interactions make only a negligible contribution to the temporally and spatially varying total diabatic heating of the atmosphere. Over the past decade, a number of observational and theoretical studies have established that in reality clouds produce radiative heating and cooling effects that are comparable to the latent heating and fluctuate on dynamically

** Present affiliation: Department of Earth and Atmospheric Sciences, Purdue University, West Lafayette, Indiana.
@ Present affiliation: Department of Atmospheric Science, Colorado State University, Fort Collins, Colorado.
+ Present affiliation: Science Applications Research Corp., NASA/GSFC, Greenbelt, Maryland.

Corresponding author address: Dr. David A. Randall, Dept. of Atmospheric Science, Colorado State University, Ft. Collins, CO 80523.

active space and time scales (Albrecht and Cox 1975; Stephens and Webster 1979; Webster and Stephens 1980; Ramanathan 1987a,b). As a result, most GCMs today include interactive (but still highly simplified) cloud parameterizations. Numerical experiments with these models have demonstrated that large-scale circulation systems are indeed sensitive to the parameterized clouds (e.g., Herman et al. 1980; Hunt et al. 1980; Meleshko and Wetherald 1981; Shukla and Sud 1981; Hunt 1982; Ramanathan et al. 1983; Charlock and Ramanathan 1985; Slingo and Slingo 1988). In addition, studies of climate change due to increasing atmospheric carbon dioxide concentrations have found that the predicted climate change significantly depends on and may even be amplified by the effects of clouds (e.g., Hansen et al. 1984; Schlesinger and Mitchell 1987; Wetherald and Manabe 1988).

Although these studies have established the importance of cloudiness for climate dynamics, it is not clear to what extent current GCMs are capable of realistically simulating the climatological distribution of cloudiness and its impact on the Earth's radiation budget. Important new observational datasets that can shed light on this question are being produced through the International Satellite Cloud Climatology Project (ISCCP; Schiffer and Rossow 1983), the First ISCCP Regional Experiment (FIRE; described by Cox et al. 1987), and the Earth Radiation Budget Experiment (ERBE; described by Barkstrom 1984).

We have analyzed the Earth radiation budget and cloudiness simulated by the UCLA/GLA GCM, and as revealed by several observational datasets. Our objectives are to identify strengths and weaknesses of the simulated cloudiness, and to demonstrate techniques for comparing GCM cloudiness simulations with observations. Although our simulations are too short to establish the model's climate with any confidence, we have compared our results with climatological data whenever possible. The signatures of cloudiness are clearly evident in both the simulated and Nimbus 7-observed solar and terrestrial radiation at the top of the atmosphere. The simulated cloudiness itself is critically compared with available observations from ISCCP and HIRS2/MSU. Emphasis is placed on the high, optically thick "anvil" cloudiness associated with deep cumulus convection. We have also analyzed the simulated cloud radiative forcing (CRF), including the forcing at the top of the atmosphere, at the Earth's surface, and across the atmosphere.

2. Computational procedure

Our results are based on the UCLA/GLA general circulation model, which is derived from the UCLA GCM developed by A. Arakawa and collaborators, and described by Suarez et al. (1983). Randall et al. (1985) presented results from the UCLA GCM, with emphasis on boundary-layer processes, especially those associated with boundary-layer stratocumulus clouds. The main differences in the present model are revised parameterizations of terrestrial and solar radiation (Harshvardhan et al. 1987). For the clear sky, the new longwave radiation parameterization includes the effects of the water vapor continuum, which leads to strong radiative cooling at low levels in humid regions such as the tropics. New parameterized cloud optical properties have also been introduced. These will be described below. In addition, we have made many minor changes to the model; their aggregate effects on the results are not so minor. A brief description of the current UCLA/GLA GCM is given by Randall et al. (1989); a summary of the cloudiness parameterization is as follows.

Three types of clouds are generated: convective "anvil" clouds, supersaturation clouds, and boundary layer stratocumulus clouds. Cumulus convection is parameterized following the theory of Arakawa and Schubert (1974), as implemented by Lord et al. (1982). Convective clouds are assumed to have negligible cloud fraction below 400 mb, so that trade cumuli, for example, have no effect on the simulated radiation field. The latent heating and drying due to shallow convective clouds are, of course, included in the model. When convection penetrates above 400 mb, an optically thick "anvil" cloud is assumed to horizontally fill the grid column, from 400 mb to the highest level reached by the convection. This crude assumption is based on observations of the upper tropospheric cloudiness associated with deep convection (e.g., Houze 1977; Webster and Stephens 1980; Ackerman et al. 1988).

Supersaturation clouds are assumed to occur when the relative humidity equals or exceeds 100%, are assigned a cloud fraction of 1, and are assumed to vertically fill the GCM layer where they occur. To the extent that the model can be said to simulate cirrus clouds, these are represented by upper-level supersaturation clouds. The anvil clouds mentioned above are intended to represent optically and geometrically thick upper-level cloud masses that would not normally be described as cirrus clouds.

The parameterized boundary-layer clouds can be arbitrarily thin; their cloud fraction is 1 when they are more than 12.5 mb deep, and decreases to zero linearly as their pressure thickness decreases from 12.5 mb to zero.

The model has a diurnal insolation cycle; cloud generation and full radiation computations are made hourly, in order to adequately resolve diurnal changes (Wilson and Mitchell 1986). The optical properties of the supersaturation and boundary-layer clouds are assumed to vary with cloud pressure–thickness and also with temperature, such that cold clouds are optically thinner than warm clouds of the same pressure–thickness. This crudely represents the "optical depth feedback" discussed by Somerville and Remer (1984).

The model's terrestrial and solar radiation parameterizations are described by Harshvardhan et al.

(1987). Off-line one-dimensional results obtained with the longwave parameterization for several clear-sky cases have been found to compare favorably with the results obtained using more accurate schemes (WMO 1984). In view of the importance of cloudiness and its interaction with radiation, however, the prescribed cloud optical properties are an important adjunct to the radiation parameterization. As described by Harshvardhan et al. (1987), the radiation parameterization can accommodate a wide variety of prescribed cloud optical properties, cloud fraction and overlap. These are considered to be inputs to the radiation code.

In the shortwave, clouds are identified with a spectrally uniform optical thickness that is proportional to the pressure thickness of the cloud. With the exception of the lowest GCM layer (the planetary boundary layer), the cloud's pressure thickness is assumed to be equal to the pressure thickness of the model layer in which it resides. For the current version of the model, this thickness is between 100–200 mb in the troposphere. For the nonabsorbing portion of the shortwave spectrum, the single scattering albedo of the cloud layer is, of course, $\omega_0 = 1.0$; in the absorbing region, a constant value of $\omega_0 = 0.99$ is assumed for the liquid droplets. This is combined with gaseous absorption, following the methods of Lacis and Hansen (1974). The asymmetry parameter is assigned a constant value of 0.85 for the delta-Eddington computation.

Theoretical and empirical evidence (Feigelson 1978; Betts and Harshvardhan 1987; Platt and Harshvardhan 1988) suggests that the coefficient of proportionality that relates the pressure thickness to the shortwave optical depth should depend on the mean cloud layer temperature, at least for supersaturation clouds at temperatures below freezing. The reason is that the condensed liquid (or ice) water content (LWC) of a cloud layer is a strong function of temperature. The LWC, in turn, can be related to the extinction coefficient, if certain assumptions are made regarding the size distribution of the cloud particles (Stephens 1978). The variable cloud optics experiments of Ramanathan et al. (1983) and Charlock and Ramanathan (1985) were carried out with the same general idea in mind. However, the relationship between the vertically integrated LWC and optical depth need not be unique over a GCM grid box, because of horizontal inhomogeneities (Harshvardhan and Randall 1985).

The temperature dependence is approximately quadratic for cold cirrus clouds, but is only a weak function of temperature above freezing. Therefore, the optical depth parameterization chosen for the model is

$$\tau_{sw} = \begin{cases} a(T_c - T_0)^2 \Delta p_c, & T_0 \leq T_c \leq -10°\text{C} \\ b\Delta p_c, & 0°\text{C} \leq T_c \end{cases} \quad (1)$$

with a linear interpolation of τ_{sw} between $-10°$ and 0°C. In (1), τ_{sw} is the shortwave optical depth, T_c is the mean cloud temperature, Δp_c is the pressure thickness of the cloud, and we have chosen $T_0 = -82.5°\text{C}$ on the basis of fitting observational data (Platt and Harshvardhan 1988). The coefficients a and b were obtained by trial and error, using satellite-derived albedos as a guide. For the current model, with Δp_c in mb, we use $a = 2.0 \times 10^{-6}$, and $b = 0.08$.

This form of τ_{sw} is inappropriate for the optically thick anvils associated with convection; a temperature-independent coefficient, $b = 0.16$, is used for anvil clouds.

The parameter most often used in the literature to characterize the longwave properties of clouds is the flux emittance. A more fundamental parameter is the infrared optical depth, τ_{ir}, which is related to the flux emittance, ϵ, by

$$\epsilon = 1 - \exp(-r\tau_{ir}), \quad (2)$$

where r is the diffusivity factor. For a fixed particle-size distribution, there is a unique relationship between the extinction coefficient at any two wavelengths, and so there is a linear relationship between the mean optical depths in the longwave and shortwave. A good rule of thumb for clouds is that $\tau_{ir}/\tau_{sw} \approx 0.5$ and $r \approx 1.5$, so that the longwave emittance can be written in the form

$$\epsilon = 1 - \exp(-\beta\tau_{sw}), \quad (3)$$

where $\beta = 0.75$. The shortwave parameterization given by (1) can then be used for the longwave as well. This approach ensures consistency between the shortwave and longwave schemes, and leads to realistic low-optical-depth behavior, which is particularly critical for cirrus clouds with very low planar albedos but moderate emittances. Of course, the emittance saturates to unity very rapidly, and the clouds then behave as black emitters in the longwave. An illustration of the relationship between planar albedo and emittance implied by (3) is given by Platt and Harshvardhan (1988).

The relationship (3) will hold with $\beta = 0.75$ only if the grid box is completely filled with cloud with a uniform value of τ_{sw}. When horizontal inhomogeneities occur, the relationship between mean quantities is not unique, even if finite cloud effects are ignored. In such a case, (3) does apply with a local τ_{sw}, but does *not* apply with an average τ_{sw}. If the mean flux emittance of a grid box is to satisfy a relationship analogous to (3), but with a mean shortwave optical depth, then the appropriate relationship is

$$\epsilon_1 = 1 - \exp(-\tilde{\beta}\bar{\tau}_{sw}), \quad (4)$$

where $\tilde{\beta}$ is an effective value of β, $\bar{\tau}_{sw}$ is the mean shortwave optical depth of the layer, and ϵ_1 is the mean emittance. Let the grid box average of the emittance be denoted by $\bar{\epsilon}$. We can show that in order to have $\epsilon_1 = \bar{\epsilon}$, the effective average value of β must be less than or equal to 0.75 (Kazarinoff 1961). The appropriate value of β will vary with both the mean value

of τ_{sw} and the distribution of τ_{sw} over the grid box. Additional complications will enter if we relax the assumption that a weighted sum of one-dimensional models represents the inhomogeneous cloud field. In any case, the consequence of choosing $\beta < 0.75$ is that thin clouds will be more transparent in the longwave for a given cloud albedo.

We now discuss the impact of the parameterization of cloud optical properties on the GCM results. The profile of the atmospheric longwave cooling rates for two standard profiles that were used in the ICRCCM project (WMO 1984) are shown in Fig. 1. The profiles have been interpolated to correspond to the UCLA/GLA GCM's 9-layer vertical structure. For both profiles, the solid line refers to the clear-sky cooling rates.

For the midlatitude winter profile, a supersaturation cloud is inserted in each of three layers marked beside the plot and the cooling rate shown for the high (dotted), middle (chain-dotted), and low (dashed) cloud by itself. For the high, middle and low clouds, the emittances of the cloudy layer computed on the basis of (1) are 0.055, 0.289 and 1.0, respectively. It is evident that the high cloud has no discernable effect, whereas the middle cloud causes some enhanced cooling in the cloud layer and reduces the cooling in the layers below. The optically black low cloud produces substantial cooling within the cloudy layer and warms the lowest model layer while leaving the layers above unaffected.

For the tropical profile, the high supersaturation cloud is not shown, since the emittance is only 0.01. The chain-dotted line shows the cooling rate for a supersaturation midlevel cloud of emittance given by (1), equal to 0.451. The low cloud (dashed) is optically black and the cooling rate profiles for the middle and low cloud are similar to the midlatitude winter case. The GCM treats convective anvils as optically black layers extending from about the 400 mb level to the top of the detrainment layer. Two cases are shown in the right panel (tropical) of Fig. 1. The profile marked with open triangles corresponds to an anvil cloud that occupies only one model layer, centered at 373.6 mb. In this situation, the cloud layer experiences cooling, and all layers below cloud base are warmed by 1–2 K day^{-1}, such that there is greatly reduced cooling in these lower layers. The profile marked with dots is for a deep anvil extending over four model layers up to 100 mb, which is the highest level of cloud formation allowed in the model. There is very strong cooling at the top of the anvil and also strong heating at the base, while the interior layers experience no net heating. This dipole structure is characteristic of deep anvils (Ackerman et al. 1988).

We have saved extensive diagnostics in order to allow a detailed analysis of the model results. These diagnostics include global "daily mean" fields based on 1-hour sampling, as well as hourly data for selected grid points. Three-dimensional fields are interpolated onto isobaric surfaces *before* time averaging. The single greatest difference between the present model and that used by Randall et al. (1985), besides the new radiation scheme and cloud optical properties, is the provision of extensive new diagnostics, particularly for diabatic processes. Among these are the clear-sky radiative fluxes, which have been saved as diagnostic results before cloud effects are accounted for; they are thus defined for all grid points, not just those that happen to be cloud-free. These clear-sky fluxes are used to determine the cloud radiative forcing. This is "Method II" discussed by Cess and Potter (1987).

Further description of the GCM is given by Randall et al. (1989).

Our results are based on the same nine-level, four-

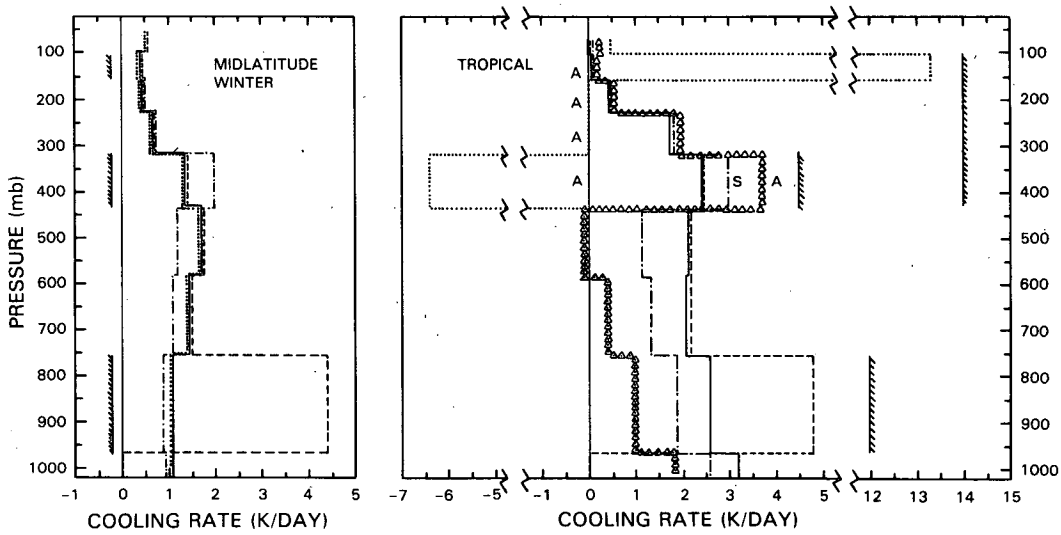

FIG. 1. The profile of the atmospheric longwave cooling rates for two standard profiles that were used in the ICRCCM project (WMO 1984). The solid lines refer to the clear-sky cooling rates.

by-five degree version of the model that was used by Randall et al. (1985). We have performed June–July and December–January simulations, starting from June 1 and December 1, respectively, using initial conditions taken from the 37-month integration discussed by Randall et al. (1985). The overall results of the present simulations are similar to those obtained by Randall et al. (1985); exceptions will be mentioned where appropriate.

3. Earth radiation budget and cloudiness

Several satellite datasets are available for comparison with the Earth radiation budget simulated by the model. We have selected the Earth Radiation Budget (ERB) data from Nimbus 7 because of its broad-band character. Although several years of wide field-of-view data are available, its horizontal resolution is inadequate for our purposes. Unfortunately, the narrow field-of-view (NFOV) data were collected for only 18 months. We have chosen the January 1980 and July 1979 Nimbus 7 ERB NFOV data for comparisons with our model results, pending availability of data from the Earth Radiation Budget Experiment (Barkstrom 1984).

A major problem in comparing model and satellite radiation fields is that the diurnal cycle is sampled differently. Nimbus 7 is a sun-synchronous polar orbiter with equator-crossing times of noon and midnight; all scanner observations away from the poles correspond to local times within an hour of those times (Jacobowitz et al. 1984). An attempt has been made to convert the albedo at satellite observation time to a mean daily value, based on a solar zenith angle response of the underlying surface, such as clouds or ocean. The GCM daily mean albedoes are obtained from hourly samples taken during the daylight hours. Because of the diurnal cycle in many fields, including insolation, surface temperature, and cloudiness, the model and satellite radiation fields are not strictly comparable. This applies for both shortwave and longwave radiation. The "daily mean" longwave satellite product is a weighted (by the ratio of the length of day to night) mean of the noon and midnight values. Over clear land regions, the emitted longwave radiation increases during the course of the day, with increasing surface temperature. This is modeled in the GCM, but not adequately accounted for in the satellite data. A more precise comparison between the simulated and observed Earth radiation budgets will be possible using ERBE data, which will combine better diurnal sampling with an effort to model the unresolved diurnal variations of outgoing longwave and albedo.

In addition to differences in temporal sampling between model and satellite, there are also differences in the numbers of observations that are averaged to form the gridded data. The Nimbus 7 output is gridded on roughly equal area targets which have a horizontal resolution of about 500 km. For each orbital pass, there are between 50 and 100 observations binned into each target area. Although these are not independent observations, since there is considerable overlap in the field of view, a typical sample consists of a wide range of scenes, many of which are partly cloudy. The GCM grid points cover roughly the same horizontal extent as the ERB target areas for the tropics and midlatitudes. There is only one realization of the radiation field per grid point per hour, however, and this realization is either clear or completely cloudy because the current model does not have a parameterization of subgrid-scale fractional cloudiness. The daily mean model quantities are obtained from these hourly samples, averaged over daylight hours only for the shortwave, and over all 24 hours for the longwave. The day-to-day variations in the simulated daily mean OLR and albedo are governed by the day-to-day changes in the duration and type of simulated cloudiness. For the satellite, on the other hand, the corresponding variations are determined by changes in the cloud fraction, top height, and optical properties near local noon and midnight.

Table 1 gives the simulated globally averaged incident solar radiation, absorbed solar radiation, planetary albedo, outgoing longwave radiation (OLR), and net radiation, for January and July. We used a solar constant of 1360 W m^{-2}. Also given are the corresponding observations from the Nimbus 7 scanners (Jacobowitz et al. 1984). The simulated Earth is "darker" and "colder" than observed, in both seasons, although the "accepted" observational values continue to evolve, and show considerable interannual variability (e.g., Stephens et al. 1981). Arking and Vemury (1984) argue that the Nimbus 7 albedo is 2.5% too high, but even allowing for this the simulated planetary albedo is about 1% less than observed. The simulated OLR is also less than observed, by 8 W m^{-2} in January and 4 W m^{-2} in July. The simulated seasonal changes in the albedo, the OLR, and the net radiation are fairly realistic. To some extent, this simply confirms that the seasonally varying Earth–sun geometry and surface boundary conditions have been correctly prescribed.

Figure 2 shows the zonally averaged monthly mean January and July planetary albedo and OLR as sim-

TABLE 1. Simulated and observed planetary radiation budgets for January and July, W m^{-2}.

	U175 January	Nimbus 7 January 80	U159 July	Nimbus 7 July 79
Incident solar radiation	352	354	329	332
Absorbed solar radiation	246	235	235	224
Planetary albedo	30	34	29	33
Outgoing longwave radiation	222	230	233	237
Net radiation	25	5	2	−14

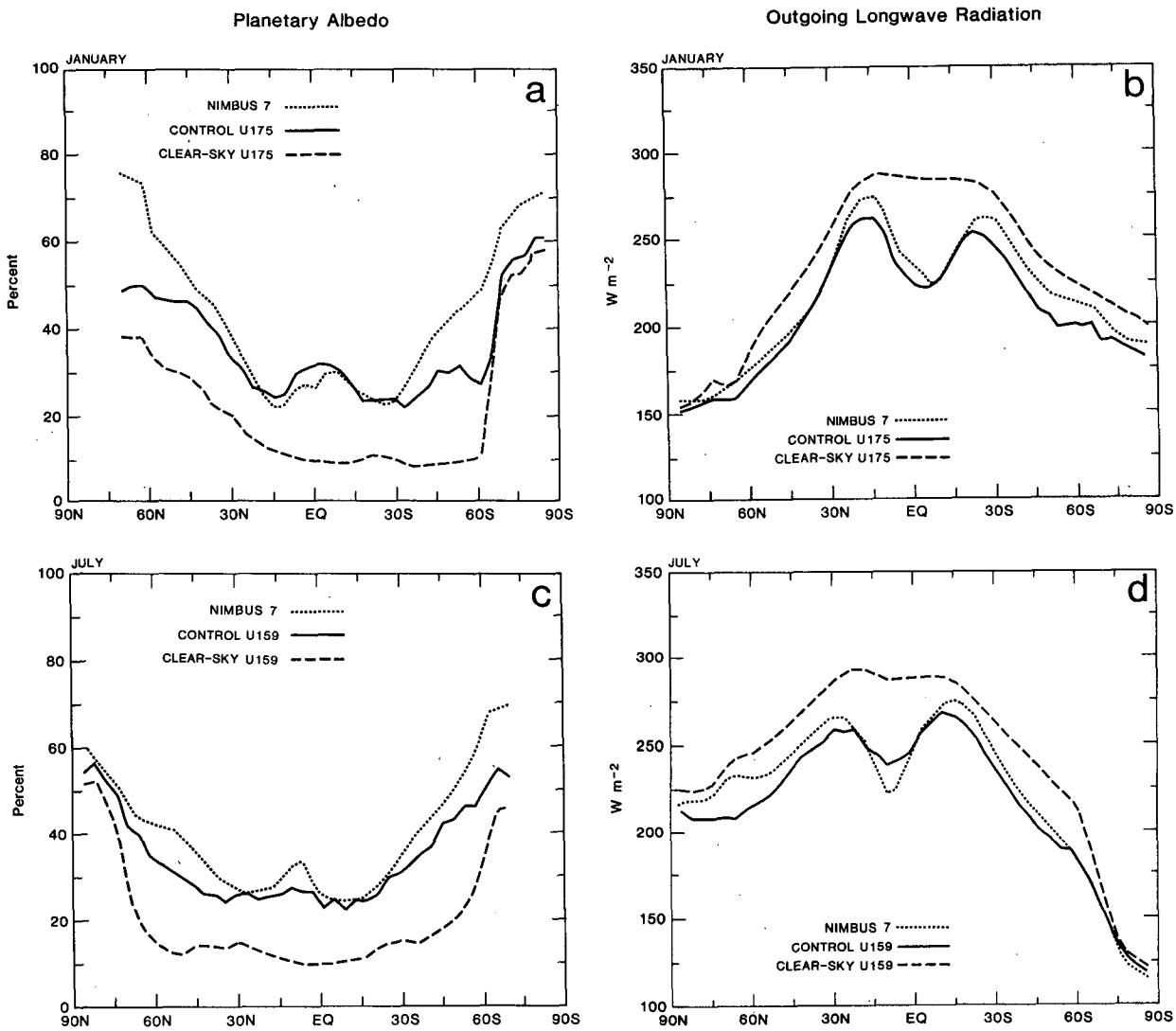

FIG. 2. The zonally averaged monthly mean January and July planetary albedo and OLR as simulated by the model, as observed by the Nimbus-7 scanner, and as simulated for the clear sky.

ulated by the model, as observed by the Nimbus-7 scanner, and as simulated for the clear sky. The observed tropical maximum of the albedo is slightly overpredicted in January, but it is almost missing in July. The corresponding observed tropical minimum of the OLR is fairly realistic in January, but is too weak in July. These results suggest that the ITCZ cloudiness is well predicted in January, but somewhat less than observed in July. Even the simulated clear-sky OLR shows a tropical minimum, due to water vapor absorption; this is consistent with the observational study of Warren and Thompson (1983).

Subtropical maxima of the OLR are correctly simulated by the model, but are about 10 W m^{-2} weaker than observed. This may indicate excessive simulated upper-level subtropical cloudiness. The observed gradient of the OLR between the ITCZ and the subtropics is considerably underestimated by the model.

The model is darker than observed in midlatitudes of both hemispheres, particularly the summer hemisphere, suggesting an underprediction of cloud amount for these regions. In the same range of latitudes, however, the model tends to underpredict the OLR; in the July simulation, this error reaches 25 W m^{-2} at 70°N. This could indicate either an *overprediction* of cloud amount, or an excessive cloud-top height. Taken together, these results suggest that deficiencies in the simulated cloudiness distribution itself are only part of the problem; it appears that the optical properties of the midlatitude clouds also require revision.

For the most part, the respective differences between the simulated values and the simulated clear-sky values

are much larger than the corresponding differences between the simulated and observed values. In other words, the parameterized cloudiness substantially improves the degree of agreement between the model's radiation budget and the observations. By this measure, the cloudiness simulations are fairly successful.

Figure 3 shows the simulated January and July zonally averaged net radiation at the top of the atmosphere; the net surface energy flux, including both radiation and turbulent sensible and latent heat fluxes; and the difference, which is the total energy flux convergence across the atmosphere. It is evident that the seasonal changes in the net surface energy flux are strongly controlled by the net radiation at the top of the atmosphere; the seasonal changes in the total energy flux convergence across the atmosphere are relatively small by comparison.

The solar and terrestrial radiation at the top of the model atmosphere fluctuate significantly on short time scales, i.e., hours to days. Figure 4a shows scatter plots of the outgoing longwave radiation (OLR) versus albedo, for a grid point in the tropical western Pacific during a simulated July. (Such detailed plots are available only at some 100 selected model grid points.) The scatter diagrams show considerable regularity, which can be explained quite readily in terms of the model's discrete structure. The hourly sampling and discrete vertical grid of the model tend to select particular zenith angles and cloud-top pressures. Clouds with particular top pressures and at particular zenith angles always look about the same, since the model does not include a fractional cloudiness parameterization; the grid boxes are either clear or completely overcast at each realization. These facts account for horizontal and vertical "stripes" of points that appear in the scatter diagrams. The vertical alignment in the upper left of the figure is a consequence of the discrete temporal sampling. The clear sky albedo is a fairly strong function of zenith angle, which takes almost the same discrete value every day at the discrete sampling hours over the month. The vertical spread is caused by thin high supersaturation clouds which do not affect the albedo but reduce the OLR. The horizontal rows in the lower right represent the tops of convective anvils which occupy discrete levels and emit at essentially the same temperature throughout the period. The horizontal spread is a consequence of the zenith-angle dependence of the cloud albedo. Points in the middle of the figure represent midlevel cloudiness. After diurnal averaging, the daily mean (shown in Fig. 4b) shows the anticipated trend from clear, high OLR-low albedo points to the bright convective anvils with low OLR. This may be compared with Fig. 4c, which is a plot from the Nimbus 7 NFOV scanner for essentially the same geographical area in July 1979. Hartmann and Short (1980) used similar plots of OLR versus albedo from satellite data to classify regions by dominant cloud type.

Figures 4d, e, f are as in Fig. 4a, b, c, but for a grid

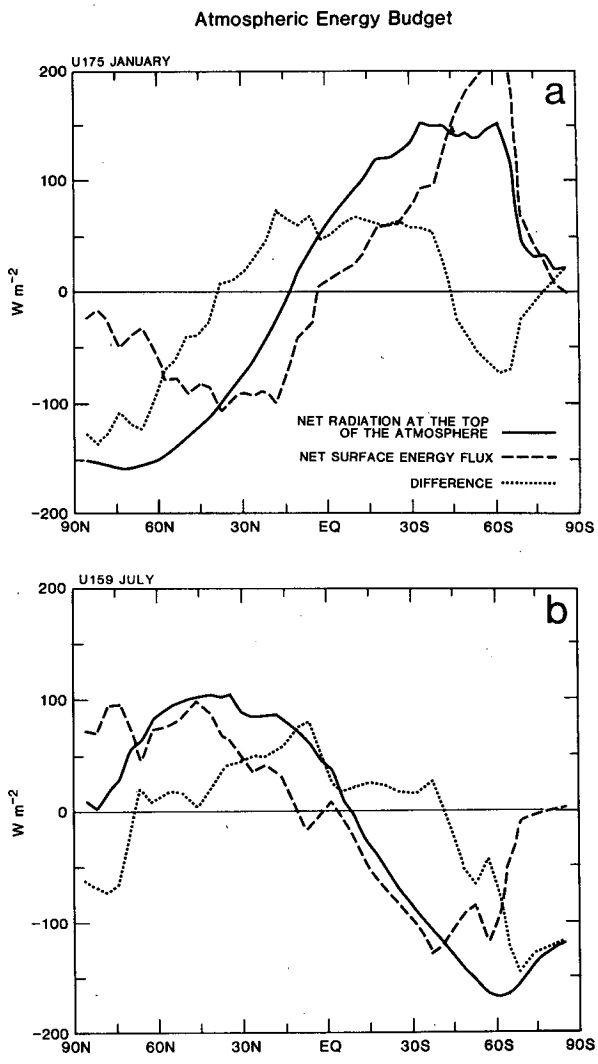

FIG. 3. The simulated January and July zonally averaged net radiation at the top of the atmosphere; the net surface energy flux, including both radiation and turbulent sensible and latent heat fluxes; and the difference, which is the total energy flux convergence across the atmosphere.

point in central North America, also in July. The hourly data for this land point is somewhat different from the ocean point. The zenith-angle dependence of the clear-sky albedo is less pronounced, and there are fewer convective anvils. The trend shown in Fig. 4e is very similar to the satellite data shown in Fig. 4f.

We now compare the simulated "total cloudiness" (defined as one minus the fraction of clear sky) with observations from ISCCP (the International Satellite Cloud Climatology Project; Schiffer and Rossow 1983), and as reported by Susskind et al. (1987). The ISCCP cloudiness is based on a threshold algorithm that makes use of both solar and terrestrial radiation, giving a "zero" or "one" for each (25 km)^2 pixel. Susskind's very different algorithm is based on solution of the ra-

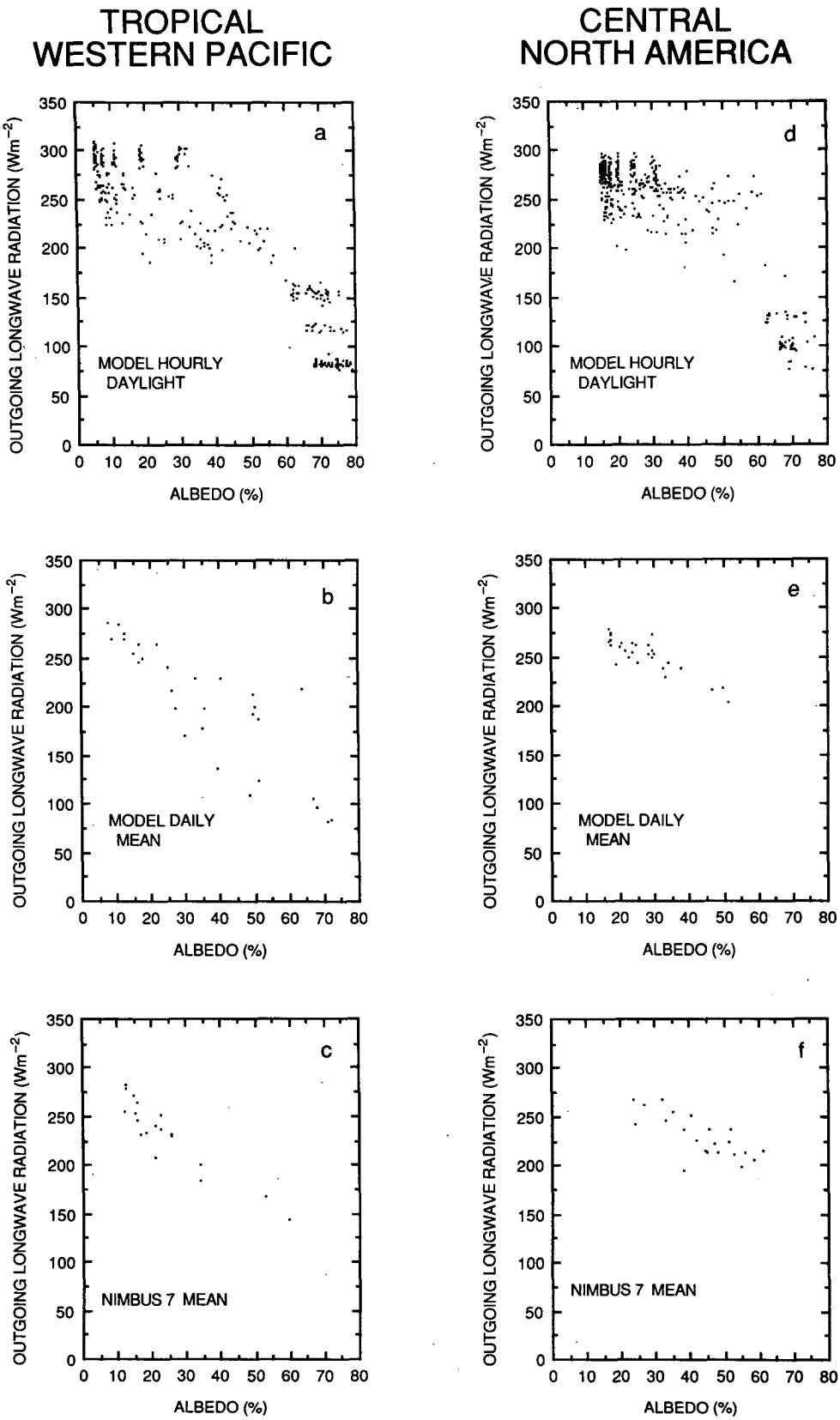

FIG. 4. (a) Scatter diagram showing simulated July outgoing longwave radiation plotted against the planetary albedo, for a tropical Pacific gridpoint. The points shown are hourly values. (b) As in (a), except using 24-h averages. (c) Nimbus 7 daily means for July 1979, and the same geographical location as in (a) and (b). (d–f) As in (a–c), but for a grid point in central North America.

diative transfer equation, to determine the cloudiness required to account for HIRS2/MSU observations of the spectrally varying terrestrial radiation. Susskind's results represent the product of the fractional cloud amount and the cloud emittance, with a horizontal resolution of about 100 km. We have averaged both sets of observations to the model's 4 by 5 degree resolution.

As will become obvious in the figures discussed below, Susskind's observed "cloud amounts" are generally much smaller than either the ISCCP observations or the model results. The reason is that, as mentioned above, Susskind's retrieval system actually yields the product of cloud amount and emittance, while the ISCCP data and the model results both represent cloud amount without regard to optical properties. The ratio of Susskind's results to the ISCCP results should therefore represent an estimate of bulk emittance of the clouds.

Figure 5 shows the simulated and observed zonally averaged total cloudiness. Before comparing the model results with the observations, we compare the two sets of observations with each other. There is fair agreement between the shapes of the ISCCP and Susskind cloud amounts, with some exceptions. Susskind's cloudiness is much smoother than that obtained in ISCCP. This is particularly striking for the tropics in January, where the ISCCP data shows a double maximum while Susskind finds a single, broader peak. This discrepancy could be due to Susskind's weighting by the emissivity, which might smooth out peaks due to optically thin clouds, or it could be due to interannual variability. Both the ISCCP data and Susskind's results show a single pronounced tropical cloudiness maximum in July. A discrepancy between the two sets of observations is found at the south pole in both seasons, where the ISCCP cloud amounts fall off much more rapidly than Susskind's. This may be due to the fact that the ISCCP algorithm relies in part on solar radiation, while Susskind's algorithm uses only terrestrial radiation. Solar radiation is of little help for cloud retrievals in the polar regions. In the polar night, there is no solar radiation, so the ISCCP algorithm has to do what it can with terrestrial radiation alone. The situation does not necessarily improve when the sun is up, since snow and ice can masquerade as low-level clouds.

The simulated cloudiness is greater, in the global mean, than observed by either ISCCP or Susskind, and it also has less meridional structure. For January, the simulated zonally averaged cloudiness appears to be particularly excessive in the northern midlatitudes. As discussed by Randall et al. (1985), much of this simulated winter cloudiness consists of very thin PBL stratus clouds over the cold continents. As shown in Fig. 2, the simulated planetary albedo is actually lower than observed for this same latitude belt. Excessive simulated cloudiness occurs over Antarctica in January and perhaps also in July. The model correctly simulates subtropical cloudiness minima, but the Northern Hemisphere minimum is not as pronounced as observed. This is consistent with the underprediction of the subtropical OLR, shown in Fig. 2. There is a simulated tropical cloudiness maximum near 10°S, which is slightly stronger than that observed during ISCCP, and also considerably smoother. The OLR and albedo are fairly realistic in this same region. A cloudiness maximum is simulated near 60°S, due to PBL stratus clouds over the ocean near Antarctica.

For July, the simulated zonally averaged midlatitude cloudiness agrees very well with the ISCCP data, for both hemispheres. Ironically, both the simulated OLR and the simulated albedo are lower than observed in these same regions. The simulated subtropical cloudiness minima are weaker than observed in both hemi-

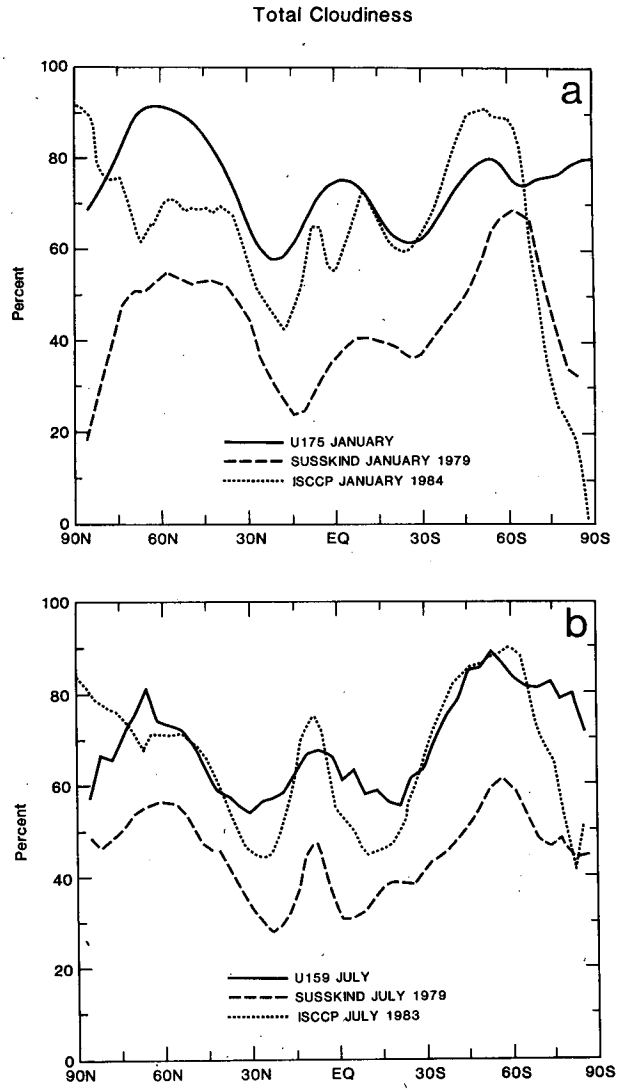

FIG. 5. The simulated and observed zonally averaged total cloudiness. The observations are from Susskind et al. (1987) and ISCCP.

spheres, which is consistent with the underprediction of the subtropical OLR. The simulated tropical maximum shifts northward in July, in agreement with the observations, but it is weaker than observed and too broad. This is consistent with the underprediction of the albedo and the overprediction of the OLR.

Maps of the simulated and observed total cloudiness for January and July are given in Fig. 6. A few successes and many deficiencies of the simulation are immediately apparent. For January, simulated cloudiness of the storm tracks in the North Atlantic and North Pacific is fairly realistic. The model does produce cloudiness minima for the major deserts of the world, throughout the year. The simulated seasonal cloudiness changes over Africa are reasonably well simulated. On the other hand, the observations clearly show zonal isopleths of the cloudiness in the equatorial Atlantic in July, while the simulation produces contours that are nearly meridional. A similar deficiency is apparent for the western Pacific in July, where the observations show a cloudiness minimum near 20°N, while the model produces a maximum. The GCM fails to simulate the observed cloudiness minimum over India in January. It produces a cloudiness maximum over Greenland in July, while the observations show a minimum there. In fact, there is a general tendency for the model to produce excessive cloudiness in mountainous regions. The observations show a cloudiness minimum over Brazil in July, which the model misses. Both the model and the observations show a ring of very high cloud amount in the stormy region north of Antarctica, throughout the year. PBL stratocumulus clouds account for much of this cloud ring.

Particularly aggravating is the model's failure to produce a clear ITCZ signal in the cloudiness, even though it does produce a fairly realistic distribution of tropical precipitation (shown by Randall et al. 1985). In addition, the simulated anvil clouds fluctuate unrealistically on subsynoptic time scales. This leads to unrealistically large simulated temporal standard deviations of the OLR and albedo in convective regions. Charlock et al. (1988) and L. Smith (personal communication 1987) have found similar unrealistically large temporal standard deviations in results from the NCAR CCM. These deficiencies of the simulated ITCZ cloudiness in the UCLA/GLA GCM apparently stem from three of our modeling assumptions. First, we have completely neglected the cloudiness associated with shallow cumulus convection. This obviously tends to reduce the ITCZ cloudiness in a very direct way, and it may also reduce it indirectly by failing to stimulate the generation of shallow convection through cloud-top radiative cooling and/or solar warming in the cloudy updrafts. Second, we have assumed that the anvils associated with deep cumuli disappear as soon as the convection itself dies out. Observations (e.g., Houze 1977; Stephens and Webster 1980) show that in reality anvil precipitation often continues for several hours after deep convection dissipates, and cirrus debris can persist for many additional hours. The model can crudely simulate this, in principle, through its moist adjustment and large-scale precipitation routines. It appears, however, that with the current grid resolution, upper-tropospheric grid boxes do not become saturated often enough in response to cumulus detrainment. We speculate that this problem might be partially alleviated by using higher resolution, since smaller grid cells would saturate more readily and local convective activity would achieve greater amplitudes. A third modeling assumption that tends to limit ITCZ cloudiness and increase short-term temporal variability is that the precipitation associated with large-scale saturation falls out instantaneously; in reality, ice crystals can spend several hours falling through the troposphere, interacting with radiation all along the way.

The simulated total cloudiness maps do not show the observed spectacular cloudiness maxima associated with marine subtropical stratocumulus clouds off the west coasts of North America, South America, southern Africa, Australia, and Spain. As discussed by Randall et al. (1985), however, the GCM does produce maxima of PBL stratocumulus cloudiness in each of these regions. These simulated PBL cloudiness maxima are obscured in the total cloudiness maps by other clouds at higher levels.

As the preceding discussion tends to show, the concept of "total cloudiness" is not very useful, because different clouds can have very different optical properties, top heights, and base heights. For this reason, it is important to examine the vertical profile of the cloudiness, and the distributions of clouds with various optical properties. Figure 7 presents the latitude–height distribution of the simulated zonally averaged cloudiness for January and July. Unfortunately, no comparable observations exist. High clouds occur frequently in the model tropics, and in middle latitudes of both hemispheres, particularly in the winter hemisphere. There is an upper-level cloudiness maximum in the tropics, reaching 35% to 40% near the 12 km level, and extending up to about 15 km. It diminishes rapidly below about the 7 km level, suggesting that it is associated with the cumulus anvils which are *prescribed* to have their bases at 400 mb. There is a sharp minimum of cloudiness at low levels in the tropics. In midlatitudes of both hemispheres, there are cloudiness maxima which are strongest near the surface, but extend upward in more or less continuous columns to about 12 km. These midlatitude clouds are associated with high relative humidity (Randall et al. 1985), and are primarily due to supersaturation and PBL stratus clouds. A column of high cloudiness and high relative humidity is consistent with upward moisture transport by large-scale vertical motions.

Figure 8 shows maps of the simulated January and July mean cumulus anvil incidence, which is the same as the fractional cloudiness associated with the anvils.

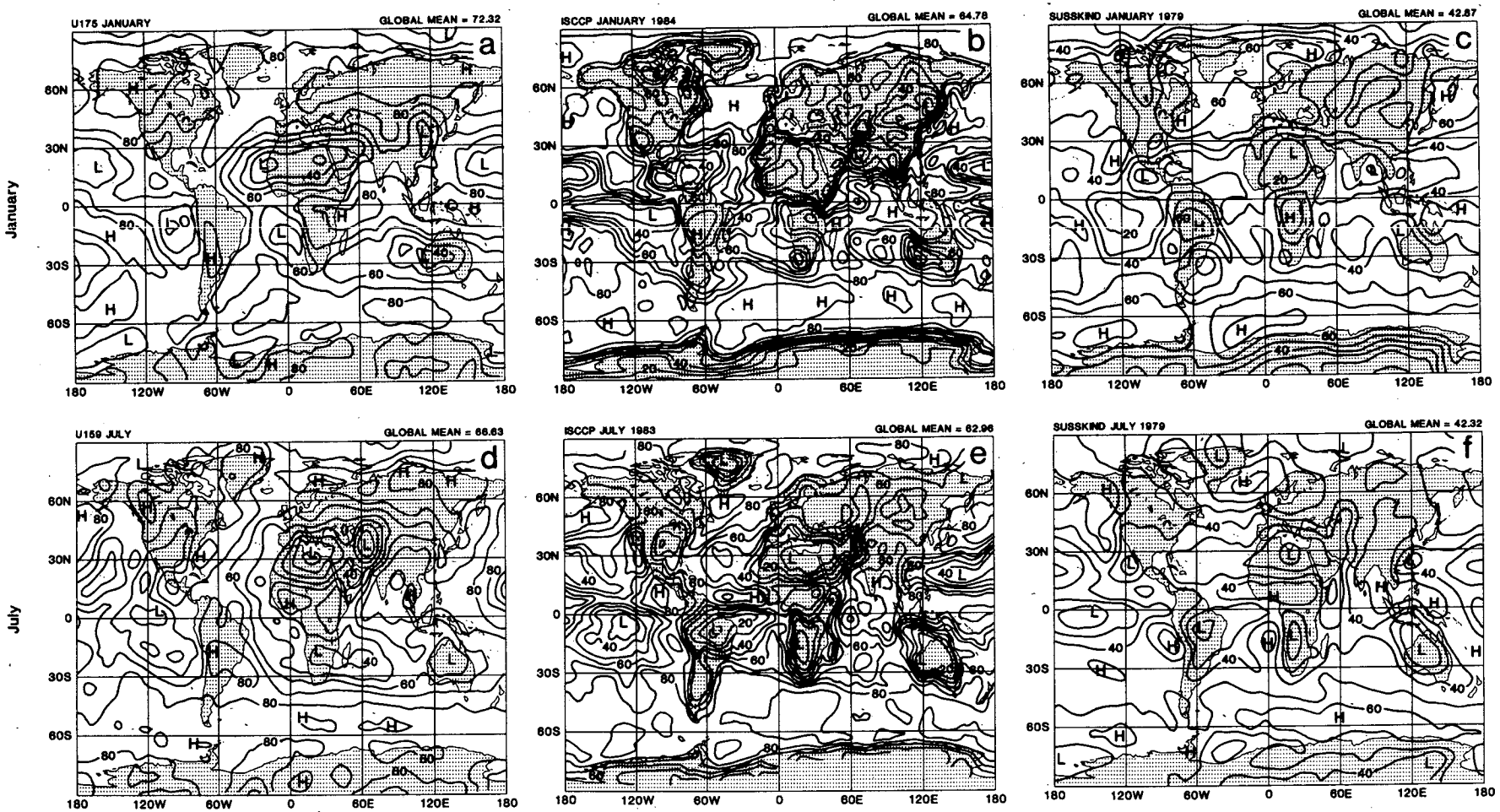

FIG. 6. Maps of the simulated and observed January (top row) and July (bottom row) total cloudiness. The observations are due to Susskind et al. (1987) and ISCCP.

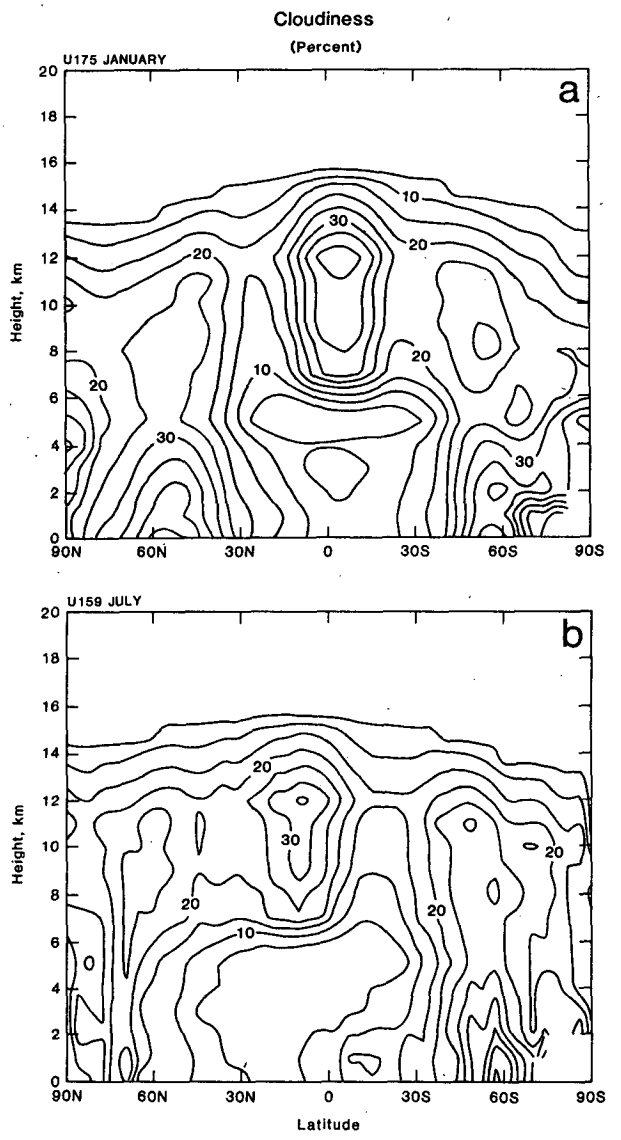

FIG. 7. The latitude-height distribution of the simulated zonally averaged cloudiness for January and July.

According to the model results, anvils cover 6% to 7% of the Earth's surface in both January and July. They are prevalent in the tropics throughout the year, and over the Northern Hemisphere continents in July. The simulated ITCZ and SPCZ experience anvil clouds up to 50% of the time. Notice that the anvil cloudiness does have more or less zonal isopleths in the tropical Atlantic, in agreement with the observed total cloudiness (Fig. 6) and in contrast with the simulated total cloudiness. Since the anvil clouds are optically thick, the simulated distribution of optically thick tropical clouds may be more realistic than the simulated distribution of all tropical clouds. The seasonal changes of convection are clearly evident over South America and Africa, and over the western equatorial Pacific. There are practically no anvils in the midlatitudes in winter; the simulations do produce some cumulus convection there, particularly in the storm tracks, but it rarely penetrates above 400 mb, so very few anvils occur.

For each simulated day, and for each grid point, we have determined the lowest pressure to which cumulus convection penetrated at any time during the day. The results have been averaged over the simulated January and July, including only those days on which convection occurred, to yield monthly maps of the cumulus cloud-top pressure. This special procedure is motivated by the considerable diurnal variation of convection over land; a simple daily mean of the cumulus cloud top pressure for a land point would typically include contributions from shallow clouds early in the day, and deeper clouds later. Such an average would be difficult to interpret. By averaging the daily maximum

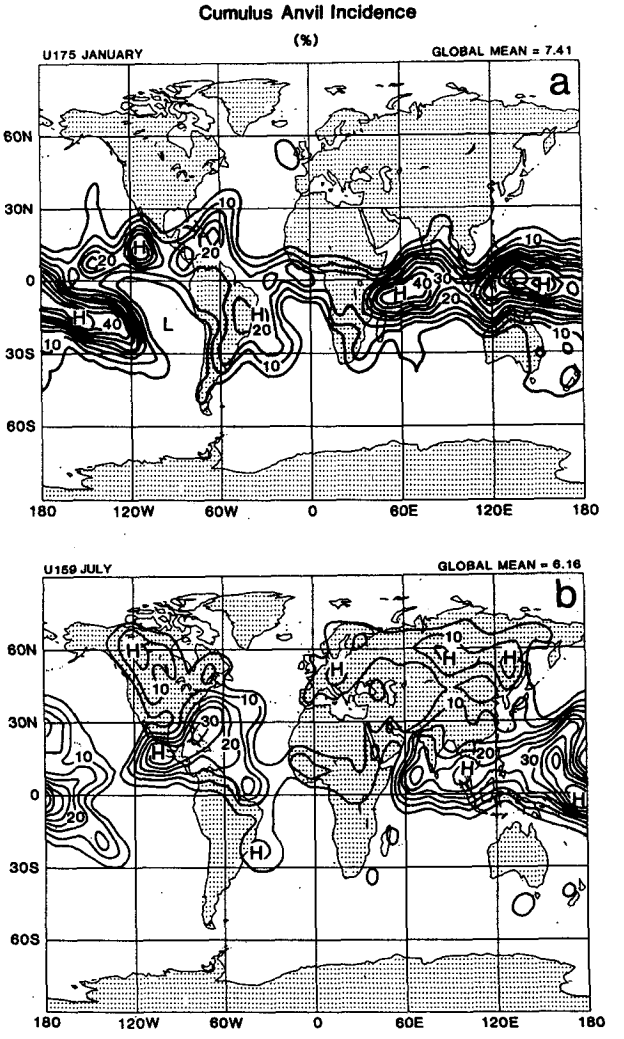

FIG. 8. The simulated January and July mean cumulus anvil incidence.

top height instead, we obtain a more meaningful indication of the top of the convection. Figure 9 shows maps of the results, for January and July. For both simulated months, the average cumulus cloud top height reaches 150 mb over the Indian Ocean, eastward into the equatorial Western Pacific, and southeastward into the SPCZ; and it exceeds 100 mb over a small region of the equatorial Western Pacific. These regions of deep convection shift northward in July and southward in January. Convection also penetrates the 150 mb surface over the Carribean Sea and Central America in July, and over South America in January.

The simulated January and July PBL stratus cloudiness were presented and discussed in detail by Randall et al. (1985), and so they are only briefly described here. The results obtained with the current model are generally similar, although the overall stratus incidence has increased. The simulated globally averaged status

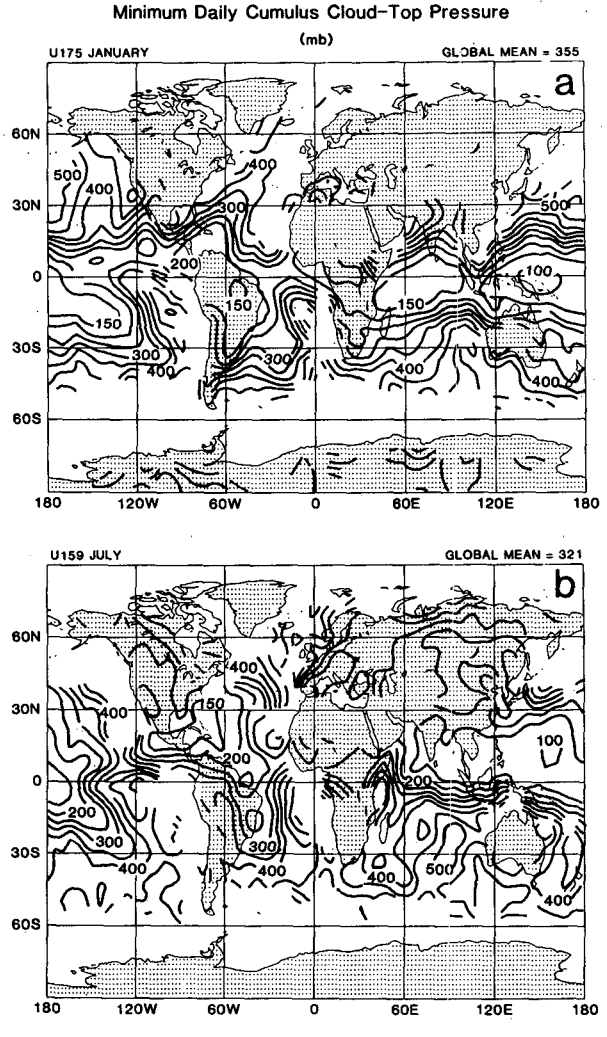

FIG. 9. January and July means of the daily minimum cumulus cloud top pressure. Contours are not drawn for regions in which cumulus convection did not occur during the month.

incidence is now between 20% and 25%, in both January and July. The current version of the GCM produces somewhat more realistic marine subtropical stratocumulus cloudiness maxima than the earlier version discussed by Randall et al. (1985). As in the 1985 model results, there is a tremendous belt of stratus clouds around Antarctica, throughout the year, associated with the strong surface winds and the latent heat flux from the ocean into the cold air spilling off the Antarctic continent. An even stronger stratus incidence maximum is found over the Northern Hemisphere continents in January, although these clouds are considerably shallower than those ringing Antarctica. The observed Arctic summer stratus is not simulated. The model correctly positions a maximum of stratus cloudiness over the United Kingdom, throughout the year.

The GCM results show a strong tendency for stratus clouds and cumulus cloud amounts to be negatively correlated with each other. This is not surprising, since stratus clouds prefer a cold PBL with a strong inversion that is usually maintained in part by large-scale sinking motion, while cumulus clouds prefer a warm PBL with a weak inversion and large-scale rising motion to promote conditional instability.

4. Cloud radiative forcing

Cloud radiative forcing (CRF) may be defined as the difference between the radiative flux (at the top of the atmosphere, say) which actually occurs in the presence of clouds, and that which would occur if the clouds were removed but the atmospheric state were otherwise unchanged (Ramanathan 1987b; Cess and Potter 1987). We also use the term CRF to denote warming or cooling tendencies due to cloud-radiation interactions. Cloud feedback is the change in CRF that accompanies a climate change (Schlesinger and Mitchell 1987). We cannot hope to understand cloud feedback until we have understood cloud forcing.

As discussed in section 2, our results are based on sampling the clear-sky radiation whether or not cloudiness actually occurs. The clear-sky values are then subtracted from the totals to obtain the CRF. Cess and Potter (1987) refer to this as "Method II." Their "Method I" is based on sampling the clear-sky fluxes only when clouds do not occur. Method I has the advantage that it more closely corresponds to the ERBE observational approach, in which a clear-sky climatology is built up by saving data only for those times when no cloud is detected by the ERBE retrieval algorithm. On the other hand, Method I has the disadvantage that the surface temperature, air temperature, and water vapor distribution undoubtedly differ systematically between cloudy scenes and clear scenes, even for a given geographical region and season. As a result, the "cloud forcing" obtained with Method I actually reflects not only the effects of the clouds them-

selves, but the additional effects of these systematic differences in noncloud variables. An important reason for such systematic differences between cloudy and clear scenes is that cloudiness often varies systematically with time of day. Method II has the advantages that it can be applied in a model that includes subgrid-scale fractional cloudiness, and it samples noncloud variables without any bias, even if they are correlated with the cloudiness. For these reasons we prefer Method II. Cess and Potter found that there were no significant differences in the results obtained with the two methods, as applied in the OSU/LLNL GCM. We find that significant differences do occur in the UCLA/GLA GCM; these will be discussed at the end of this section.

It is useful to consider separately the CRF of the Earth's surface, the atmosphere, and the planet as a whole (at the top of the atmosphere). Before discussing geographical distributions, we present the global means. Table 2 gives the simulated globally averaged solar (or "shortwave"), terrestrial ("longwave"), and net CRF, for the Earth as a whole, for the atmosphere, and for the surface. The simulated planetary shortwave CRF is a cooling of about 56 W m^{-2} for January and 47 W m^{-2} for July; and the planetary longwave CRF is a warming of about 31 W m^{-2} for January and 28 W m^{-2} for July, giving a net cooling of about 24 W m^{-2} for January and 19 W m^{-2} for July. These values are similar to those obtained by Ramanathan (1987b) with the CCM, and are comparable to the typical GCM results presented in Table 4 of Cess and Potter (1987). (The UCLA/GLA results given in that table are different from the present results because we have revised the model's cloud optical properties, primarily by reducing the infrared opacity of cold supersaturation clouds.)

Table 3 summarizes the simulated and observed globally averaged cloud radiative forcings at the top of the atmosphere. The HIRS2/MSU observations analyzed by Wu and Susskind (personal communication 1988) give a longwave CRF of 23 W m^{-2} for January 1979 and 21 W m^{-2} for July 1979. Nimbus 7 observations discussed by Ardanuy et al. (1988) give a longwave planetary cloud forcing of 23 W m^{-2} for December–January–February 1980 and 25 W m^{-2} for June–July–August 1979. The simulated globally averaged longwave planetary CRF is thus 5 to 10 W m^{-2} higher than observed, for both seasons. This is consistent with the model's underprediction of the observed OLR.

TABLE 2. Simulated CRF for January and July in W m^{-2}.

	Solar	Terrestrial	Net
U175 January cloud forcing			
Top	−56	32	−24
Interior	4	2	6
Surface	−60	30	−30
U159 July cloud forcing			
Top	−47	28	−19
Interior	3	1	4
Surface	−51	27	−24

TABLE 3. Simulated and observed planetary CRF for January and July in W m^{-2}.

	Solar	Terrestrial	Net
January planetary cloud forcing			
UCLA/GLA GCM (U175)	−56	32	−24
HIRS2/MSU		23	
Nimbus 7 (DJF)		23	
July planetary cloud forcing			
UCLA/GLA GCM (U159)	−47	28	−19
HIRS2/MSU		21	
Nimbus 7 (JJA)		25	

These comparisons of global means at the top of the atmosphere mean very little, however. Even if perfect agreement were found, large differences could occur in the geographical distributions, in the partitioning of the CRF between the atmosphere and the Earth's surface, and also in the vertical distribution of the CRF within the atmosphere. Figure 10 shows the zonally averaged solar, terrestrial, and net CRF at the top of the atmosphere, across the atmosphere, and at the Earth's surface, for both January and July. Figure 11 shows maps of the simulated net CRF for January (top) and July (bottom) at the top of the atmosphere (left), at the surface (center), and across the atmosphere (right).

The net CRF at the top of the atmosphere is a strong cooling in the summer hemisphere, a weak cooling in the tropics, and a weak warming in the winter hemisphere. This meridional structure represents most of the spatial variability, although longitudinal variations are also quite noticeable in the tropics. Figure 11 makes it clear that the global mean net cooling of the Earth by CRF is a relatively small negative residual, resulting from the near cancellation of positive and negative contributions in different parts of the globe. In a different climatic regime, this residual might well be positive.

Both solar and terrestrial CRF strongly affect the energy balance of the Earth's surface. Globally, the net surface CRF is a cooling in both seasons, but again this is a residual effect. The surface is cooled by cloud shadows, especially in the tropics and the summer hemisphere, and it is warmed by downward emission of longwave radiation from cloud base, especially where the clouds are low. These effects give a cooling throughout the year in the tropics; in middle latitudes, they give a warming of the surface in winter, and a cooling in summer. Near both poles, however, the simulated surface CRF is a warming in local summer.

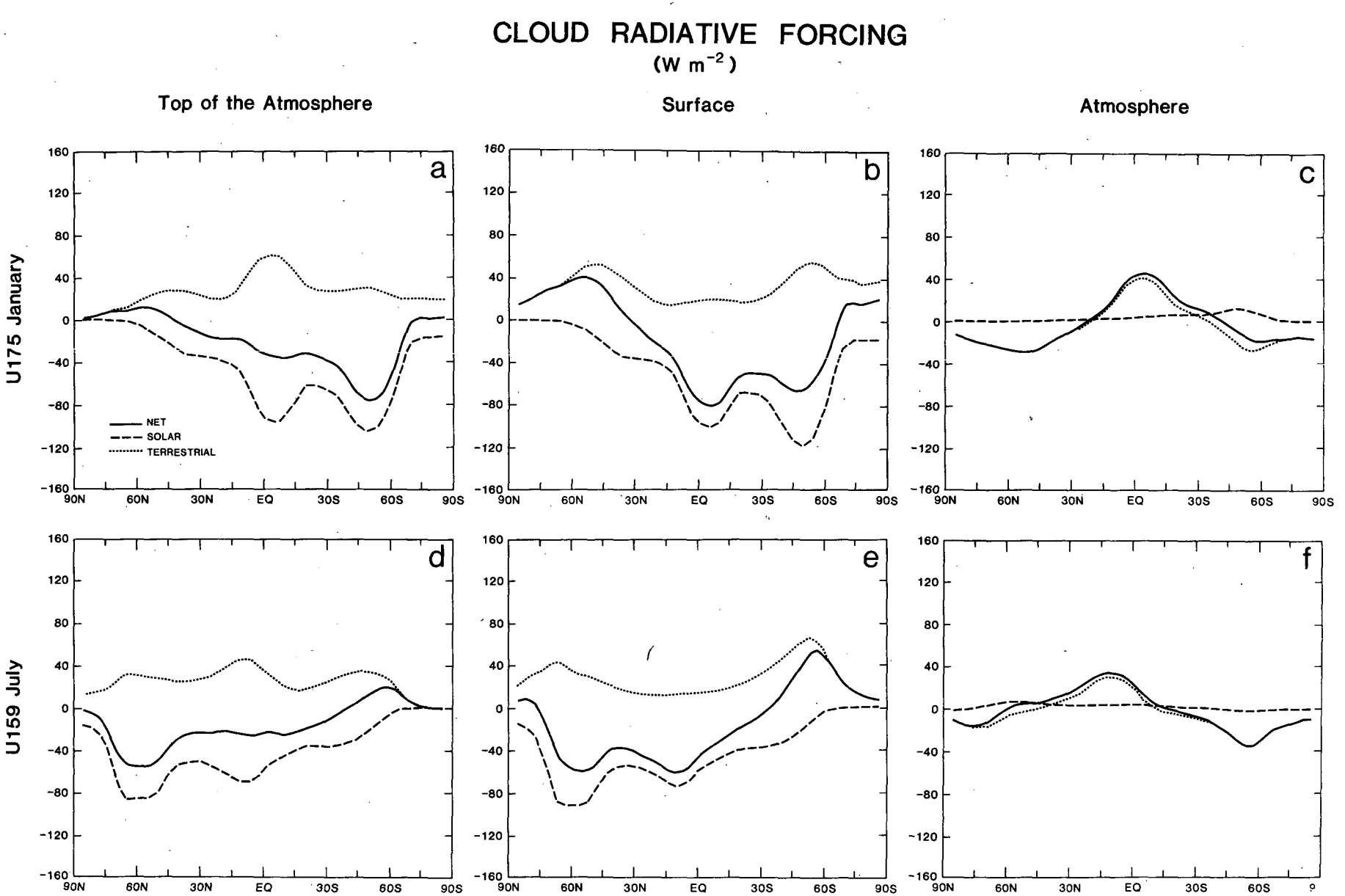

FIG. 10. January (top row) and July (bottom row) zonally averaged cloud radiative forcing at the top of the atmosphere, at the Earth's surface, and across the atmosphere. In each panel, the dashed line is the solar CRF, the dotted line is the terrestrial CRF, and the solid line is the net CRF. Positive values are always in the sense of warming.

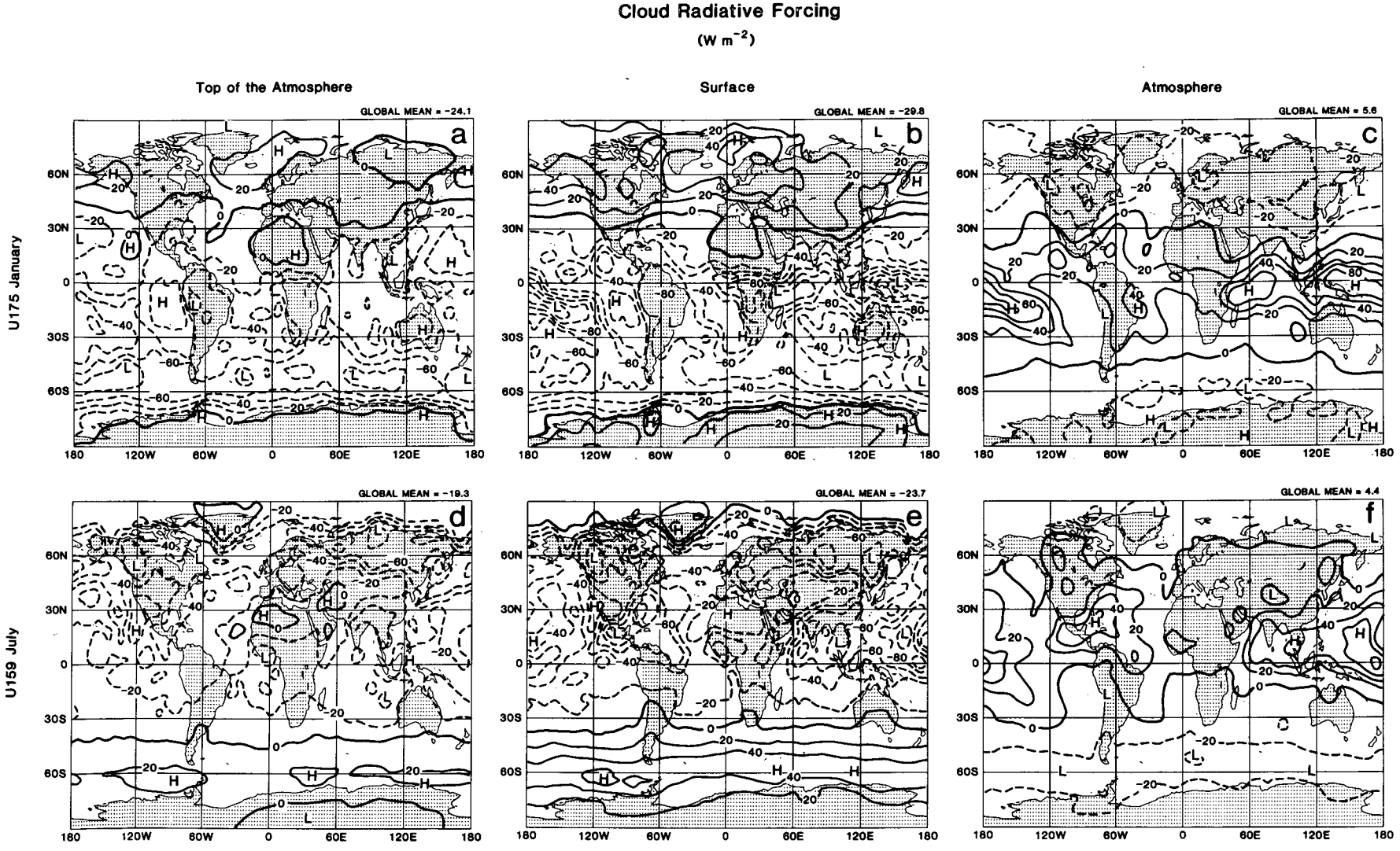

FIG. 11. Maps of the January (top row) and July (bottom row) cloud radiative forcing at the top of the atmosphere, at the Earth's surface, and across the atmosphere. Positive values are always in the sense of warming.

There the high ice albedo limits solar warming of the surface whether or not clouds are present.

Since the heat capacity of the land surface is small, the cooling of the tropical and summer hemisphere land surface by clouds has to be balanced on short time scales (hours to days) by corresponding reductions in the surface sensible and latent heat fluxes. This would tend to reduce the intensity of cumulus convection. Since a significant component of the cloudiness is produced by the convection, this represents a negative feedback loop. A similar argument would apply, with much longer time scales, for the oceanic regions. Further discussion is given by Randall et al. (1989).

The radiative effects of the clouds on the atmosphere itself are more complex. The atmosphere absorbs slightly more solar radiation in the presence of clouds; but, more importantly, clouds cause it to emit less longwave radiation to space (especially for high clouds) and somewhat more to the Earth's surface, especially for low clouds. The atmosphere is hardly affected by the solar CRF, which is felt almost entirely at the Earth's surface. Through longwave CRF, the clouds radiatively warm or cool the atmosphere depending on the altitude at which they occur (e.g., Cox 1969). A high cold cloud tends to warm the atmosphere, because it absorbs intense radiation from the Earth's surface, while emitting only weakly. In contrast, a low warm cloud tends to cool the atmosphere, because it emits strongly both upward and downward, while absorbing primarily on its lower side. Since high clouds are common in the tropics, while low clouds occur frequently in middle latitudes and near the poles, the zonally averaged atmospheric CRF (hereafter ACRF) is a warming in the tropics and a cooling in higher latitudes, thus demanding a poleward heat transport by the atmosphere, in addition to that required by latent heating and clear-sky radiative cooling. The net atmospheric CRF is dominated by a warming in the tropics, with a maximum magnitude of about 50 W m^{-2}; and a cooling in the higher latitudes of both hemispheres, with a maximum magnitude of about 30 W m^{-2}. These effects are almost entirely due to longwave radiation. The zonally averaged warming is strongest at 10°S in January, and at 10°N in July; it follows the seasonal shifts of the tropical convention.

The zonal variations in the ACRF, which are associated with the zonal asymmetries of the precipitation and large-scale vertical motion, are just as strong as the meridional variations. This is particularly striking in the tropics and subtropics, and is in agreement with the ideas of Albrecht and Cox (1975) and Stephens and Webster (1980). The ACRF is a warming in regions of large-scale ascent where high clouds occur (e.g., in the equatorial western Pacific), and a cooling in regions of large-scale descent, where low clouds occur (e.g., off the coast of California in July). The warming favors further rising motion, which tends to reinforce the high cloudiness (Starr and Cox 1985a,b), while the cooling favors large-scale sinking motion, which is favorable for low-level marine stratocumulus clouds (Lilly 1968). The strongest whole-column warming due to ACRF is about 80 W m^{-2}, in the equatorial Western Pacific, which is equivalent to a precipitation rate of 3 mm day^{-1}. Wherever latent heating is important, the ACRF provides additional warming; and where evaporation exceeds precipitation, the ACRF provides cooling. The radiative effects of the clouds on the atmosphere thus reinforce the effects of the latent heating associated with cloud formation. These results suggest that the ACRF plays a major role in atmospheric energetics, and acts as a strong positive feedback on the large-scale vertical motion field that selects the cloud type and top height. Further evidence for this is provided by Randall et al. (1989) who discuss the roles of radiative and latent heating in the model atmosphere.

There is a remarkably close balance between the ACRF-induced warming in the tropics and the midlatitudes of the summer hemisphere, and the ACRF-induced cooling in the subtropics and the winter hemisphere. The globally averaged ACRF is very small compared to the local warming and cooling maxima: the clouds radiatively warm the global atmosphere by a mere 5 W m^{-2}, even though local warming and cooling maxima are an order of magnitude larger. Although it is to be expected that the ACRF warms in some places and cools in others, it is remarkable that the warming and cooling cancel as closely as they do. Another way of looking at this is that the clouds themselves are close to radiative equilibrium, but only in a global sense. The atmosphere as a whole is of course radiatively cooled, and *individual* cloudy regions are radiatively warmed or cooled at significant rates, but *collectively* the cloudy portions of the atmosphere are close to radiative equilibrium. Perhaps this is a matter of chance.

The vertical distribution of the ACRF within the atmosphere is of considerable interest, and is discussed by Randall et al. (1989). Unfortunately, the atmospheric component of the cloud radiative forcing cannot be corroborated by satellite measurements.

We now investigate the differences between the simulated clear-sky absorbed solar radiation and clear-sky outgoing longwave radiation, which were determined using Method II of Cess and Potter (1987) and used in the discussion of CRF given above, and those that are obtained with Method I. Figure 12 shows the July-averaged differences in the zonal means of the clear-sky absorbed solar radiation and the clear-sky outgoing longwave radiation, as functions of latitude. In the tropics, Method I gives up to 30 W m^{-2} more solar absorption than Method II. Elsewhere the differences in the clear-sky absorbed solar radiation are smaller and may not be significant. At all latitudes, the zonally averaged clear-sky OLR is a few watts per square meter greater with Method I than with Method II; the differences are small but very systematic. Because the total solar and terrestrial radiation do not differ between the

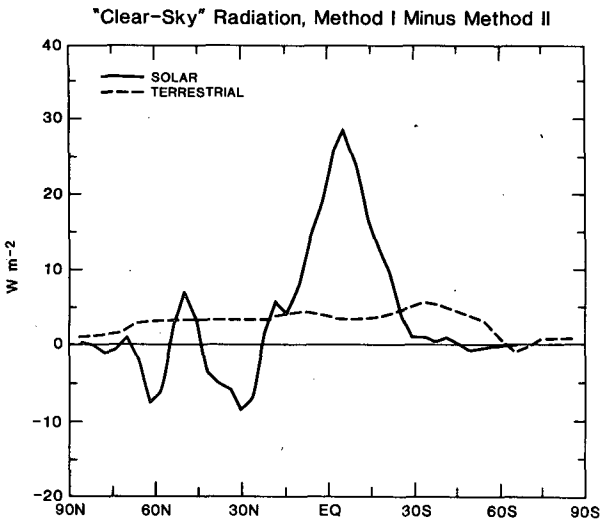

FIG. 12. Solid line: Difference in the zonally averaged clear-sky absorbed solar radiation as determined by Methods I and II of Cess and Potter (1987). Dashed line: Same for outgoing longwave radiation.

two methods, these differences in the clear-sky fluxes correspond directly to differences in the shortwave and longwave CRF. Specifically, less clear-sky absorption corresponds to weaker solar CRF, and less clear-sky OLR corresponds to weaker terrestrial CRF. These results from the UCLA/GLA GCM differ considerably from those obtained by Cess and Potter (1987) with the OSU/LLNL GCM.

The differences in the clear-sky absorbed solar radiation are due to the model's tendency to produce more cloudiness at night than during the day (discussed by Randall et al. 1985). To understand this, consider an idealized case in which the clear-sky absorbed solar radiation is a constant S during the day, and 0 at night, and suppose that day and night are of equal length. Method II gives a mean clear-sky absorbed solar radiation of $S/2$. The results obtained with Method I depend on the day–night differences in cloudiness, however. If cloudiness is distributed equally during the day and night, Method I also gives a mean of $S/2$. If clouds occur only during the day and not at night, Method I gives a mean of 0. If clouds occur only during the night, and not at all during the day, Method I gives a mean of S, which is twice as large as the mean given by Method II. The simulated diurnal cycle of cloudiness over the topical oceans is such that there is a tendency for high clouds to occur more often at night or when the sun is low in the sky. Method I does not sample this weak clear-sky solar absorption, but Method II does. As a result, for this cloud regime Method I yields more time-averaged clear-sky solar absorption than Method II. The differences are largest in the tropics because that is where brightest clouds occur. Since the results of Cess and Potter (1987) show little difference between the clear-sky solar absorption obtained with Methods I and II, we conclude that the diurnal variations of cloudiness and surface temperature simulated by the OSU/LLNL GCM differ significantly from those obtained with the UCLA/GLA GCM. Further discussion of the UCLA/GLA GCM's simulation of the diurnal variability of the hydrologic cycle will be given in a forthcoming paper.

The differences in the clear-sky OLR arise mainly from two effects. One is that, in the model results, cloud-free columns tend to contain slightly less water vapor, on the average, than cloudy columns. Since Method I samples only cloud-free columns, while Method II samples all columns, there is a tendency for Method I to find drier columns that emit more longwave radiation. A second point is that over land the UCLA/GLA GCM tends to produce low stratocumulus clouds at night, when the ground is cold and the OLR is relatively small (Randall et al. 1985). Method I does not sample these low values of the OLR, but Method II does. We have determined that both of these factors contribute significantly to the excess clear-sky OLR found by Method I, as shown in Fig. 12. We lack sufficient information to explain why Cess and Potter (1987) find negligible differences in the clear-sky OLR obtained with Methods I and II. We can only speculate that the longwave radiation parameterization of the OSU/LLNL GCM may be less sensitive to water vapor, and the model may not produce a diurnal cycle of cloudiness.

5. Summary and concluding remarks

Although many deficiencies remain, the simulated Earth radiation budget and cloudiness results presented in this paper are in reasonable agreement with the observations. This is not really the point, however. Even if a future version of the GCM exactly reproduces the available observations, this achievement will show only that the formulation of the model is correct; it will not in itself provide any additional understanding of how the atmosphere works. To increase understanding, the GCM must be used in controlled numerical experiments (e.g., Lorenz 1967). The results of some experiments are reported by Randall et al. (1989), and are used to evaluate some aspects of the model's cloudiness parameterizations.

Future work to quantify the influence of the cloud radiative forcing on the atmospheric general circulation and climate will focus on comparison of model results with data just now becoming available from ERBE, ISCCP, and FIRE; and on development of improved physical parameterizations for cloudiness and convection. The present results are encouraging, but suggest many areas where improvement is needed.

Among the most serious deficiencies of the present study is that we have only one simulated January and one simulated July. Although the computing resources currently available to us do not allow it, a single integration spanning five or more annual cycles would be very useful, for several reasons: 1) Several realizations of each month would provide a stronger statistical basis

for our conclusions. 2) A multiyear integration would reveal the model's interannual variability. 3) The dynamics of seasonal change could be analyzed.

A companion paper presents a further analysis of the effects of atmospheric cloud radiative forcing on the large-scale circulation and the hydrologic cycle (Randall et al. 1989), with particular attention to the *mechanisms* through which the clouds exert their influence.

Acknowledgments. This research has been supported by NASA's Climate Program. Computing resources were provided by the Numerical Aerodynamic Simulation Program at NASA/Ames. H. L. Kyle, J. Susskind, and M.-L. Wu provided satellite data.

APPENDIX

A Numerical Experiment on the Effects of Continuum Absorption

"E-type" or "continuum" absorption by water vapor strongly influences the radiative cooling rates in the lower troposphere, especially in the tropics (e.g., Cox 1973). Since there is no universally accepted theoretical explanation for the continuum, and all representations of it are essentially empirical, there is great uncertainty as to how it should be incorporated into radiation models. The longwave radiation parameterization currently used in the UCLA/GLA GCM includes a representation of the continuum absorption (Harshvardhan et al. 1987), but the parameterization that it replaced did not (Schlesinger 1976). When the new parameterization was implemented, we noted some dramatic changes in the simulated low-level longwave cooling rates, particularly in the tropics. These changes were traced to the introduction of the continuum. We performed an experiment to investigate the implications of these changes, by omitting the effects of the water vapor continuum in the GCM's longwave radiation parameterization, for a June–July case. We refer to this as the NOETYPE experiment. The June–July integration discussed in the body of this paper is used as the control. Ramanathan (1987a) has also discussed the effects of the water vapor continuum on the large-scale circulation of the atmosphere.

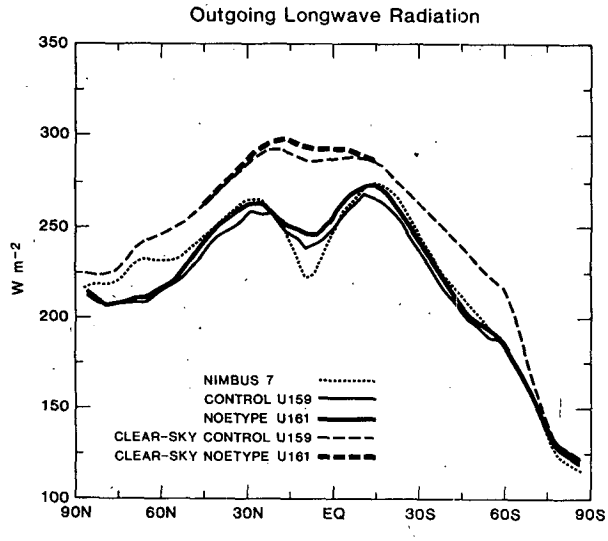

FIG. 13. Zonally averaged outgoing longwave radiation in the NOETYPE experiment and the control. Also shown are the corresponding clear-sky fluxes for both simulations, and the Nimbus 7 observations.

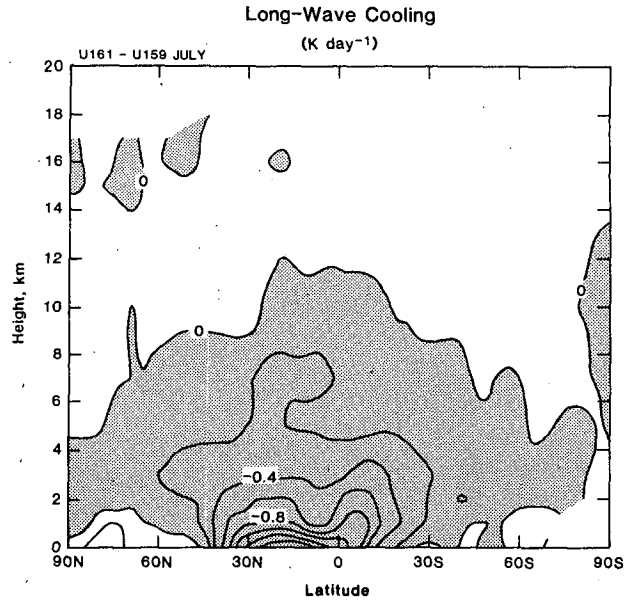

FIG. 14. Change in zonally averaged longwave cooling rate between NOETYPE and control.

As shown in Fig. 13, continuum absorption reduces the simulated zonally averaged tropical clear-sky OLR by 10 W m^{-2}. This is in accord with the observations of Warren and Thompson (1983). The total OLR is reduced by a similar amount. When the e-type absorption is neglected, the longwave cooling of the tropical lower tropospheric diminishes (Fig. 14). This decreased cooling may be thought of as the forcing for this experiment. The total radiative forcing of the atmosphere increases by 16 W m^{-2}, resulting in warmer temperatures (Fig. 15); the zonally averaged 200 mb geopotential height increases by 60 m in the tropics, and 75 m in midlatitudes of the Northern Hemisphere. The changes in the temperature field are accompanied by substantial shifts in the winds, as the model adjusts to maintain approximate thermal-wind balance. The zonal wind becomes more westerly (or less easterly) in the tropics at upper levels.

The most spectacular changes occur in the surface energy balance, however. The net upward longwave radiation at the surface increases by 20.6 W m^{-2} in the global mean. As shown in Fig. 16, this increased longwave cooling of the surface is nearly balanced by reductions in the surface latent heat flux (-14.2 W m^{-2}) and the surface sensible heat flux (-3.1 W m^{-2}). Thus one effect of the continuum cooling due to water vapor is to increase the upward flux of water vapor from the

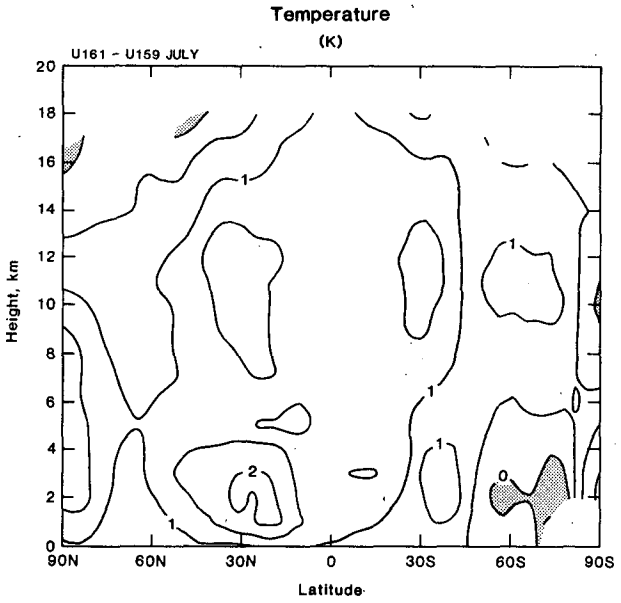

FIG. 15. Change in zonally averaged temperature between NOETYPE and control.

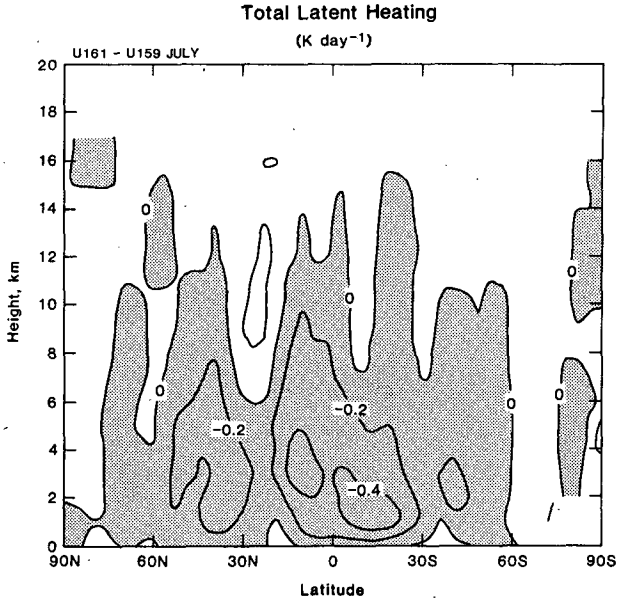

FIG. 17. Change in zonally averaged total latent heating between NOETYPE and control.

surface to the atmosphere. In this way, the surface moisture flux is somewhat self-promoting.

The reduced evaporation in the experiment leads to 10% less precipitation in the global mean; most of the change occurs over the tropical oceans. Moist convective activity generally diminishes, as shown in Fig. 17 by the difference in the total latent heating. Continuum absorption thus exerts a significant effect on the hydrologic cycle over the tropical oceans.

The surface longwave cloud radiative forcing (CRF) shifts towards warming, in the experiment, by 12.8 W m^{-2}. This is not due to an increase in low cloudiness; in fact, the low cloudiness actually decreases slightly in the experiment. Instead, the surface longwave CRF increases because the *contrast* between the greenhouse effect of low clouds and that of water vapor in the clear sky increases quite dramatically if clear-sky continuum absorption in the atmospheric window is eliminated. The atmospheric longwave CRF decreases by 10.4 W m^{-2}; clouds thus produce a slight cooling of the atmosphere in the experiment, whereas in the control they produce a slight warming (Randall et al. 1988).

The results of this experiment show the tremendous impact of the continuum on the surface energy balance. This will become much more important in future coupled ocean–atmosphere models.

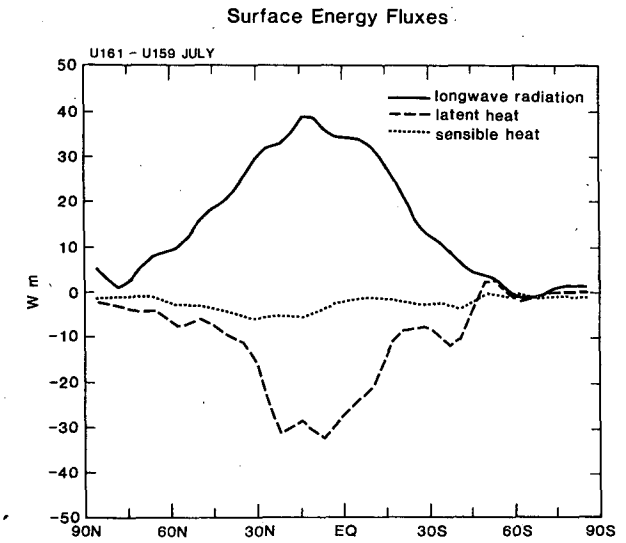

FIG. 16. Zonally averaged changes in net surface longwave radiation, surface latent heat flux, and surface sensible heat flux, between NOETYPE and control.

REFERENCES

Ackerman, T. P., K.-N. Liou, F. P. J. Valero and L. Pfister, 1988: Heating rates in tropical anvils. *J. Atmos. Sci.*, **45**, 1606–1623.

Albrecht, B., and S. K. Cox, 1975: The large-scale response of the tropical atmosphere to cloud modulated infrared heating. *J. Atmos. Sci.*, **32**, 16–24.

Arakawa, A., and W. H. Schubert, 1974: The interaction of a cumulus cloud ensemble with the large-scale environment. Part I. *J. Atmos. Sci.*, **31**, 674–701.

Ardanuy, P. E., L. L. Stowe, A. Gruber, M. Weiss and C. S. Long, 1989: Longwave cloud radiative forcing as determined from Nimbus-7 observations. *J. Climate*, in press.

Arking, A., and S. Vemury, 1984: The NIMBUS 7 ERB data set: A critical analysis. *J. Geophys. Res.*, **89**, 5089–5097.

Barkstrom, B. R., 1984: The Earth Radiation Budget Experiment (ERBE). *Bull. Amer. Meteor. Soc.*, **65**, 1170–1185.

Betts, A. K., and Harshvardhan, 1987: Thermodynamic constraint on the cloud liquid water feedback in climate models. *J. Geophys. Res.*, **92**, 8483–8485.

Cess, R. D., and G. L. Potter, 1987: Exploratory studies of cloud radiative forcing with a general circulation model. *Tellus*, **39A**, 460–473.

Charlock, T. P., and V. Ramanathan, 1985: The albedo field and

cloud radiative forcing produced by a general circulation model with internally generated cloud optics. *J. Atmos. Sci.*, **42,** 1408–1429.

——, K. M. Cattany-Carnes and F. Rose, 1988: Fluctuation statistics of outgoing longwave radiation in a general circulation model and in satellite data. *Mon. Wea. Rev.*, **116,** 1540–1554.

Cox, S. K., 1969: Radiation models of midlatitude synoptic features. *Mon. Wea. Rev.*, **97,** 637–651.

——, 1973: Infrared heating calculations with a water vapor pressure broadened continuum. *Quart. J. Roy. Meteor. Soc.*, **99,** 669–679.

——, D. S. McDougal, D. A. Randall and R. A. Schiffer, 1987: FIRE—The First ISCCP Regional Experiment. *Bull. Amer. Meteor. Soc.*, **68,** 114–118.

Feigelson, E. M., 1978: Preliminary radiation model of a cloudy atmosphere. Part 1: Structure of clouds and solar radiation. *Contrib. Atmos. Phys.*, **51,** 203–229.

Hansen, J., A. Lacis, D. Rind, G. Russell, P. Stone, I. Fung, R. Ruedy and J. Lerner, 1984: Climate sensitivity: Analysis of feedback mechanisms. *Climate Processes and Climate Sensitivity,* Maurice Ewing Series (5), J. E. Hansen and T. Takahashi, Eds., Amer. Geophys. Union, 130–163.

Harshvardhan, and D. A. Randall, 1985: Comments on "The parameterization of radiation for numerical weather prediction and climate models". *Mon. Wea. Rev.*, **113,** 1832–1833.

——, R. Davies, D. A. Randall and T. G. Corsetti, 1987: A fast radiation parameterization for general circulation models. *J. Geophys. Res.*, **92,** 1009–1016.

Hartmann, D. L., and D. A. Short, 1980: On the use of earth radiation budget statistics for studies of clouds and climate. *J. Atmos. Sci.*, **37,** 1233–1250.

Herman, G., M.-L. Wu and W. T. Johnson, 1980: The effects of clouds on the earth's solar and infrared radiation budgets. *J. Atmos. Sci.*, **37,** 1251–1261.

Houze, R. A., 1977: Structure and dynamics of a tropical squall-line system. *Mon. Wea. Rev.*, **105,** 1540–1567.

Hunt, G. E., 1982: On the sensitivity of a general circulation model climatology to changes in cloud structure and radiative properties. *Tellus,* **34,** 29–38.

——, V. Ramanathan and R. M. Chervin, 1980: On the role of clouds in the general circulation of the atmosphere. *Quart. J. Roy. Meteor. Soc.*, **106,** 213–215.

Jacobowitz, H., R. J. Tighe and the NIMBUS 7 Experiment Team, 1984: The Earth radiation budget derived from the NIMBUS 7 ERB Experiment. *J. Geophys. Res.*, **89D,** 4997–5010.

Kazarinoff, N. D., 1961: *Analytical Inequalities.* Holt, Rienhart and Winston, 89 pp.

Lacis, A. A., and J. E. Hansen, 1974: A parameterization for the absorption of solar radiation in the Earth's atmosphere. *J. Atmos. Sci.*, **31,** 118–133.

Lord, S. J., W. C. Chao and A. Arakawa, 1982: Interaction of a cumulus cloud ensemble with the large-scale environment. Part IV: The discrete model. *J. Atmos. Sci.*, **39,** 104–113.

Lorenz, E. N., 1967: The nature and theory of the general circulation of the atmosphere. World Meteorological Organization, No. 218, TP115, 161 pp.

Meleshko, V. P., and R. T. Wetherald, 1981: The effect of a geographical cloud distribution on climate: A numerical experiment with an atmospheric general circulation model. *J. Geophys. Res.*, **86,** 11 995–12 014.

Platt, C. M. R., and Harshvardhan, 1988: The temperature dependence of cirrus extinction—implications for climate feedback. *J. Geophys. Res.*, **93,** 11 051–11 058.

Ramanathan, V., 1987a: Atmospheric general circulation and its low-frequency variance: Radiative influences. *Short and Medium-Range Weather Prediction,* T. Matsuno, Ed., Collection of Papers Presented at the WMO/IUGG NWP Symp., Tokyo, 151–175.

——, 1987b: The role of Earth radiation budget studies in climate and general circulation research. *J. Geophys. Res.*, **92,** 4075–4095.

——, E. J. Pitcher, R. C. Malone and M. L. Blackmon, 1983: The response of a spectral general circulation model to refinements in radiative processes. *J. Atmos. Sci.*, **40,** 605–630.

Randall, D. A., J. A. Abeles and T. G. Corsetti, 1985: Seasonal simulations of the planetary boundary layer and boundary-layer stratocumulus clouds with a general circulation model. *J. Atmos. Sci.*, **42,** 641–676.

——, Harshvardhan, D. A. Dazlich and T. G. Corsetti, 1989: Interactions among radiation, convection, and large-scale dynamics in a general circulation model. *J. Atmos. Sci.*, **46,** 1943–1970.

Schiffer, R. A., and W. B. Rossow, 1983: The International Satellite Cloud Climatology Project (ISCCP): The first project of the World Climate Research Programme. *Bull. Amer. Meteor. Soc.*, **64,** 779–784.

Schlesinger, M. E., 1976: A numerical simulation of the general circulation of atmospheric ozone. Ph.D. dissertation, UCLA, 375 pp.

——, and J. F. B. Mitchell, 1987: Climate model simulations of the equilibrium climatic response to increased carbon dioxide. *Rev. Geophys.*, **25,** 760–798.

Shukla, J., and Y. Sud, 1981: Effect of cloud-radiation feedback on the climate of a general circulation model. *J. Atmos. Sci.*, **38,** 2337–2353.

Slingo, A., and J. M. Slingo, 1988: The response of a general circulation model to cloud longwave radiative forcing. Part I: Introduction and initial experiments. *Quart. J. Roy. Meteor. Soc.*, in press.

Somerville, R. C. J., and L. A. Remer, 1984: Cloud optical thickness feedbacks in the CO_2 climate problem. *J. Geophys. Res.*, **89,** 9668–9672.

Starr, D. O'C., and S. K. Cox, 1985a: Cirrus clouds. Part I: A cirrus cloud model. *J. Atmos. Sci.*, **42,** 2663–2681.

——, and ——, 1985b: Cirrus clouds. Part II: Numerical experiments on the formation and maintenance of cirrus. *J. Atmos. Sci.*, **42,** 2682–2694.

Stephens, G. L., 1978: Radiation profiles in extended water clouds. Part II: Parameterization schemes. *J. Atmos. Sci.*, **35,** 2123–2132.

——, and P. J. Webster, 1979: Sensitivity of radiative forcing to variable cloud and moisture. *J. Atmos. Sci.*, **36,** 1542–1556.

——, G. G. Campbell and T. H. Vonder Haar, 1981: Earth radiation budgets. *J. Geophys. Res.*, **86,** 9739–9760.

Suarez, M. J., A. Arakawa and D. A. Randall, 1983: Parameterization of the planetary boundary layer in the UCLA general circulation model: Formulation and results. *Mon. Wea. Rev.*, **111,** 2224–2243.

Susskind, J., D. Reuter and M. T. Chahine, 1987: Cloud fields retrieved from analysis of HIRS2/MSU sounding data. *J. Geophys. Res.*, **92,** 4035–4050.

Warren, S. G., and S. L. Thompson, 1983: The climatological minimum in tropical outgoing infrared radiation: Contributions of humidity and clouds. *Quart. J. Roy. Meteor. Soc.*, **109,** 169–185.

Webster, P. J., and G. L. Stephens, 1980: Tropical upper tropospheric extended clouds: Inferences from Winter MONEX. *J. Atmos. Sci.*, **37,** 1521–1541.

Wetherald, R. T., and S. Manabe, 1988: Cloud feedback processes in a general circulation model. *J. Atmos. Sci.*, **45,** 1397–1415.

Wilson, C. A., and J. F. B. Mitchell, 1986: Diurnal variation and cloud in a general circulation model. *Quart. J. Roy. Meteor. Soc.*, **112,** 347–409.

World Meteorological Organization, 1984: The intercomparison of radiation codes in climate models (ICRCCM). *WCP-93,* Geneva, 37 pp.